About the dynamics and morphology of single ellipsoidal bubbles in liquids

Mikaelian David[a], Larcy Aurélie[a], Cockx Arnaud[b], Wylock Christophe[a], Haut Benoît[a]

[a] Laboratory Transfers, Interfaces and Processes (TIPs), CP 165/67, Université Libre de Bruxelles, Av. F. D. Roosevelt 50, 1050 Brussels, Belgium
[b] Université de Toulouse; INSA, UPS, INPT; LISBP, Av. de Rangueil 135, F-31077 Toulouse, France

Abstract

A data postprocessing method for an imaging technique based on shadowgraphy is presented in this paper. It enables a precise analysis of the dynamics of a bubble rising in a liquid. The morphology of the bubble is also precisely analyzed by determining an appropriate threshold for the binarization of the images. Experiments with single ellipsoidal bubbles rising in various water-glycerol mixtures, with an oscillatory trajectory and without interface wobbling, are analyzed. It is rigorously shown that the minor axis and the mass center velocity vector of a bubble are aligned in the case of a zigzag and an helical motion of the bubble. The interface curvature radii at the front and at the rear of a bubble are determined and, in the case of a zigzag motion of the bubble, a correlation for their ratio is proposed. In the vertical motion of the bubbles, a pulsation at twice the frequency of the horizontal motion is identified in the case of a zigzag motion of the bubbles. In the case of a helical motion of the bubbles, such a pulsation cannot be

Preprint submitted to Elsevier *July 3, 2014*

This is the preprint version of a manuscript published in Experimental Thermal and Fluid Science 64 (2015), p. 1-12.
Permalink: http://dx.doi.org/10.1016/j.expthermflusci.2015.01.013

identified in the vertical motion of the bubbles.

Keywords: ellipsoidal bubbles, shadowgraphy, oscillatory trajectory, curvature, correlation

---

1. Introduction

Non-spherical bubbles of a few millimeters rising in liquids with a non-linear trajectory are commonly encountered in many industrial applications, like absorption towers, waste water treatment, fermentation, etc. Their dynamics and morphology highly influence the efficiency of these industrial applications because they control the mixing and the mass transfers between the gas and the liquid. Therefore, the dynamics and the morphology of bubbles moving in various liquids have been extensively investigated, theoretically, numerically and experimentally, for many years (Rosenberg (1950), Haberman and Morton (1953), Saffman (1956), Hartunian and Sears (1957), Moore (1958, 1963, 1965), Aybers and Tapucu (1969a,b), Grace et al. (1976), Clift et al. (1978), Ryskin and Leal (1984), Dandy and Leal (1986), Blanco and Magnaudet (1995), Duineveld (1995), Lunde and Perkins (1997), Brüker (1999), Ellingsen and Risso (2001), Mougin and Magnaudet (2002), de Vries et al. (2002), Haut and Cartage (2005), Shew et al. (2006), Mougin and Magnaudet (2006), Magnaudet al. (2006), Magnaudet and Mougin (2007), Zenit and Magnaudet (2008), Wylock et al. (2011), Legendre et al. (2012), Cano-Lozano et al. (2012) and Mikaelian et al. (2013)). As the continuation of all these studies, three topics on the

This is the preprint version of a manuscript published in Experimental Thermal and Fluid Science 64 (2015), p. 1-12.
Permalink: http://dx.doi.org/10.1016/j.expthermflusci.2015.01.013

dynamics and the morphology of single ellipsoidal bubbles rising in liquids are investigated in this paper.

First, for a complete description of the dynamics of an ellipsoidal bubble rising in a liquid with a non rectilinear trajectory, it is necessary to characterize the relative orientation of the bubble minor axis and the bubble mass center velocity vector (referred to as the velocity vector of the bubble hereafter). Such a characterization was first investigated in the work of Saffman (1956). In his work, Saffman assumed that the velocity vector of a bubble rising with a zigzag or an helical trajectory is aligned with the bubble minor axis. This assumption has only been roughly validated by comparison with its own experimental results and the experimental results of Miyagi (1925). In the work of Ellingsen and Risso (2001), the rise of 2.5 mm ellipsoidal bubbles in water with a zigzag or a flattened helix motion was recorded by a camera. The possible alignment of the minor axis and the velocity vector of the bubbles was discussed and corroborated by observing the match between the recorded bubble projections and the bubble projections calculated by supposing a 2.5 mm ellipsoidal bubble rising in a water with its minor axis parallel to its velocity vector. In the work of Ellingsen and Risso (2001), the alignment of the minor axis and the velocity vector of a bubble was also validated by determining experimentally the direction of its minor axis when its velocity vector was vertical. To the best of our knowledge, the assumption that the velocity vector of an ellipsoidal bubble rising with a zigzag or helical motion is aligned with the bubble minor axis has never been experimentally

This is the preprint version of a manuscript published in Experimental Thermal and Fluid Science 64 (2015), p. 1-12.
Permalink: http://dx.doi.org/10.1016/j.expthermflusci.2015.01.013

validated by a direct comparison of these two vectors, determined at the successive positions of the bubble during its rise.

Second, the absence of symmetry of the bubble interface between the front and the rear of the bubble (referred hereafter as fore-and-aft asymmetry) was observed numerically in Ryskin and Leal (1984) and experimentally in Duineveld (1995) and Zenit and Magnaudet (2008). The influence of the bubble fore-and-aft asymmetry on its motion was highlighted in Cano-Lozano et al. (2012) and Zenit and Magnaudet (2008). It is therefore important to characterize it. To the best of our knowledge, no experimental evaluation of the interface curvature radii at the front and the rear of the bubble is available for a bubble rising in a liquid.

Third, it was observed in Ellingsen and Risso (2001) that a 2.5 mm ellipsoidal bubble does not rise in water with a constant vertical velocity. Indeed, there is a weak pulsation in the vertical motion of the bubble, with a frequency twice the frequency of the zigzag motion of the bubble. In Shew et al. (2006), a pulsation in the bubble vertical motion at twice the frequency of the bubble horizontal motion was observed for millimetre-sized bubbles rising in water with a zigzag motion. Such a pulsation has not been identified in the helical motion of these bubbles. To the best of our knowledge, the presence of a possible pulsation in the bubble vertical motion has not been investigated for bubble sizes larger than 2.5 mm.

These three topics are investigated in this work using the experimental set-up presented in Mikaelian et al. (2013) and a new data postprocessing

This is the preprint version of a manuscript published in Experimental Thermal and Fluid Science 64 (2015), p. 1-12.
Permalink: http://dx.doi.org/10.1016/j.expthermflusci.2015.01.013

method. This experimental set-up is based on a shadowgraphy technique. Bubbles of various sizes are generated in a column filled with a water-glycerol mixture and their rises are recorded by a camera. Perspective effects are avoided using two convergent lenses. The high resolution and large field of view of the set-up enable simultaneous analysis of the dynamics and the morphology of the generated bubbles. More details are provided in Section 2.1. The steps in studying these three topics are:

1. to develop a postprocessing method of raw images recorded using the experimental set-up described above, in order to analyze the dynamics and the morphology of single ellipsoidal bubbles rising freely with a non linear trajectory in a column filled with liquid;
2. to apply this data postprocessing method on raw images obtained in Mikaelian et al. (2013) in order
   (a) to determine the directions of the minor axis and the velocity vector of a bubble and to analyze if they are aligned, in the cases of a zigzag motion and a helical motion of the bubble;
   (b) to evaluate the curvature radii of the liquid-gas interface at the front and at the rear of a bubble and to establish a correlation for the ratio of these two curvature radii as a function of its Eötvös and the Morton numbers;
   (c) to analyze whether or not a pulsation can be identified in the dynamics of the vertical motion of the mass center of a bubble of equivalent diameter larger than 2.5 mm, in the cases of a zigzag

This is the preprint version of a manuscript published in Experimental Thermal and Fluid Science 64 (2015), p. 1-12.
Permalink: http://dx.doi.org/10.1016/j.expthermflusci.2015.01.013

motion and a helical motion of the bubble.

2. Materials and methods

2.1. Experimental set-up

The experimental set-up used in Mikaelian et al. (2013) is represented in Fig. 1 and described briefly hereafter.

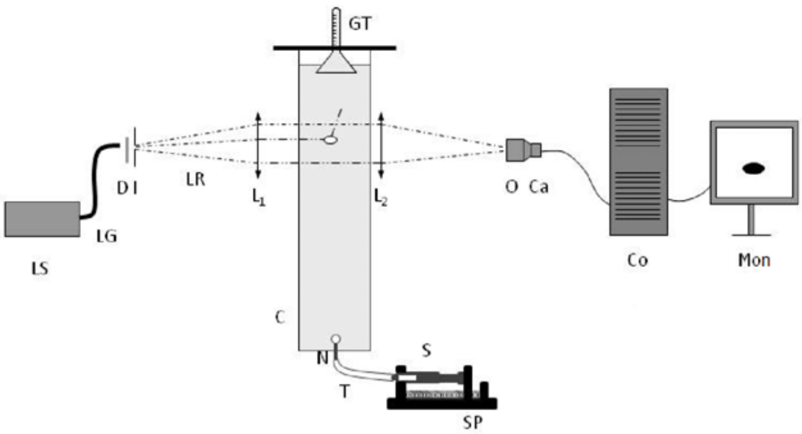

Figure 1: Sketch of the experimental set-up used in Mikaelian et al. (2013). LS : light source, LG : light guide, D : diffuser, I : iris, LR : light rays, L_1: first lens, L_2 : second lens, O : objective, Ca : camera, Co : computer, Mon : monitor, SP : syringe pump, S : syringe, T : tube, N : needle, C : column, GT : graduated tube or bubble collector.

A Plexiglas column ($0.13 * 0.13 * 1.5$ m^3) is filled with various water-glycerol mixtures. Bubbles are generated by injecting gas into the liquid at the bottom of the column using various injection devices (depending on the desired bubble diameter). The injection device is either a capillary tube or a capillary tube followed by a hypodermic needle (T and N in Fig. 1). The gas is introduced into the capillary tube with a gas-tight syringe (Hamilton,

This is the preprint version of a manuscript published in Experimental Thermal and Fluid Science 64 (2015), p. 1-12.
Permalink: http://dx.doi.org/10.1016/j.expthermflusci.2015.01.013

1005LT or 1010LT), conveying gas into the tube at a flow-rate controlled by a syringe pump (kdScientific, kds250). During the experiment, a chain of bubbles is generated with the time interval between the generations of two successive bubbles controlled by the syringe pump. A "bubble collector" consisting of a graduated glass tube (interior diameter 0.009 m) sealed to a glass funnel (GT in Fig. 1) is used at the top of the column. Gas volumes up to 4 ml can be measured, with a precision of 0.05 ml.

The imaging set-up comprises a white light source (Dolan-Jenner, Fiber-Lite DC-950, 150 W Quartz halogen lamp), a light guide (Olympus, KL-BL13/1000, 3 mm in diameter, 1000 mm long), a light diffuser, an iris, two convergent lenses (achromatic lenses, 800 mm focal length and 150 mm in diameter), an objective (Nikon, Micro Nikkor 60 mm), and a high speed camera (Teledyne Dalsa, Falcon1.4M100). It is placed at a vertical distance of 0.98 m from the bottom of the column in order to ensure that bubbles reach their terminal morphology and dynamics at the height of the camera and in order to be far enough from the liquid surface. The maximum frame rate of this camera is 100 Hz when images with a size of 1024 x 1400 pixels are recorded. Reducing the image size enables the camera's frame rate to be increased. In this work, the images are recorded at 150 Hz with an exposure time of 100 μs. The sizes of the recorded images are either 300 x 1400 pixels, 400 x 1400 pixels or 500 x 1400 pixels, with 1400 pixels placed in the vertical direction.

The two convergent lenses (L_1 and L_2 in Fig. 1) are used in order to

This is the preprint version of a manuscript published in Experimental Thermal and Fluid Science 64 (2015), p. 1-12.
Permalink: http://dx.doi.org/10.1016/j.expthermflusci.2015.01.013

avoid perspective effects. The distance between the first lens and the iris (I in Fig. 1) is equal to the focal length of the first lens. Therefore, the light rays of the light source are parallel after having crossed the lens and the depth of field during image recording is much larger than the characteristic sizes of the experimental set-up. The distance between the convergent lenses and the column wall is approximately 10 cm. The camera is positioned after the second lens at a distance lower than the focal length of the lens. The camera is connected to a computer. The length scale of the recorded images is determined using a meshed transparent paper fixed onto one side of the column. It is equal to 10 pixels/mm. The camera focus setting is realized by placing a capillary tube in the middle of the column.

When a bubble is between the two lenses, as shown in Fig. 2, the projection of the bubble onto the recording plane of the camera (RPC) appears black on the images recorded by the camera. Indeed, the light rays impacting the bubble are diffused and deviated due to the refractive index difference between the liquid and the air. In the following, the projection of a bubble on the RPC is simply referred to as the "bubble projection".

2.2. Experimental data set

Ten experiments that were carried out in Mikaelian et al. (2013) are postprocessed in this work. The complete experimental procedure used to carry out these experiments and an extensive description of the precision of the experimental set-up were presented in Mikaelian et al. (2013). In

This is the preprint version of a manuscript published in Experimental Thermal and Fluid Science 64 (2015), p. 1-12.
Permalink: http://dx.doi.org/10.1016/j.expthermflusci.2015.01.013

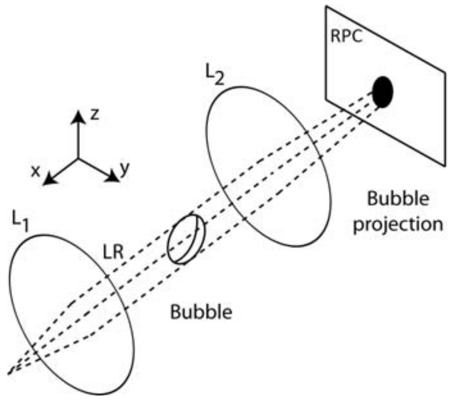

Figure 2: Real bubble and its projection onto the recording plane of the camera (RPC).

the selected experimental set, bubbles with various sizes were generated and images of their rises in various water-glycerol mixtures were recorded, as described in Section 2.1. Bubbles rising with either a zigzag or a helical motion and without interface wobbling were observed. For each generated bubble, a minimum of 70 images covering two or three periods of the zigzag or helical motion of the bubble were recorded.

The ten experiments were characterized using the Eötvös (Eo), the Morton (Mo), the Reynolds (Re) and the Weber (We) numbers of the bubbles. These dimensionless numbers have been calculated, for a given experiment, by:

$$\mathrm{Eo} = \frac{\rho g < d_e >^2}{\gamma} \tag{1}$$

$$\mathrm{Mo} = \frac{g\mu^4}{\rho\gamma^3} \tag{2}$$

$$\mathrm{Re} = \frac{\rho < v >< d_e >}{\mu} \tag{3}$$

This is the preprint version of a manuscript published in Experimental Thermal and Fluid Science 64 (2015), p. 1-12.
Permalink: http://dx.doi.org/10.1016/j.expthermflusci.2015.01.013

$$\mathrm{We} = \frac{\rho < v >^2 < d_e >}{\gamma} \tag{4}$$

where ρ is the density of the water-glycerol mixture [kg m^{-3}], g is the gravity acceleration [m s^{-2}], $< d_e >$ is the mean equivalent diameter of the bubbles generated during the considered experiment [m], γ is the surface tension of the liquid-gas interface [N m^{-1}], μ is the dynamic viscosity of the water-glycerol mixture [kg m^{-1}s^{-1}] and $< v >$ is the mean vertical velocity of the bubbles generated during the considered experiment [m s^{-1}].

For each of the ten experiments, μ and γ were measured experimentally at the temperature of the water-glycerol mixture in the bubble column. ρ was evaluated at this temperature using the data of Perry and Green (1997) and Bosart and Snoddy (1928). In order to evaluate $< v >$ for a given experiment, the vertical velocity (v) of each bubble generated during this experiment was evaluated by taking the slope of the linear fit of the successive vertical coordinates of the bubble projection mass center (z_b) as a function of the time, and $< v >$ was then calculated. For the evaluation of $< d_e >$, it was assumed that all the bubbles of an experiment have the same volume. The total volume of all the bubbles generated during an experiment was measured with the bubble collector at the top of the column. It was corrected by taking into account the hydrostatic pressure difference between the top of the column and the height of the camera. This corrected volume was divided by the number of bubbles of the experiment in order to obtain the volume of a single bubble, V_b [m^3], at the height of the camera. From this

This is the preprint version of a manuscript published in Experimental Thermal and Fluid Science 64 (2015), p. 1-12.
Permalink: http://dx.doi.org/10.1016/j.expthermflusci.2015.01.013

volume, the mean equivalent diameter $< d_e >$ of the bubbles was calculated by $< d_e >= (6V_b/\pi)^{1/3}$.

The characteristics of the ten experiments of Mikaelian et al. (2013) are presented in Tab. 1. More details about the evaluation of the uncertainties of the dimensionless numbers and the evaluation of the measurement error of $< d_e >$ can be found in Mikaelian et al. (2013).

This is the preprint version of a manuscript published in Experimental Thermal and Fluid Science 64 (2015), p. 1-12.
Permalink: http://dx.doi.org/10.1016/j.expthermflusci.2015.01.013

	Exp.	Eo	Mo	Re	We	$< d_e >$ (mm)
Water	1	0.89 ± 0.02	1.17×10^{-11}	854 ± 12	2.65±0.05	2.55±0.02
Water with 20%wt of glycerol	2	0.91 ± 0.02	$1.56 \times 10^{-10} \pm 4 \times 10^{-12}$	427 ± 8	2.38±0.05	2.49±0.02
	3	2.62 ± 0.06	$1.55 \times 10^{-10} \pm 4 \times 10^{-12}$	644 ± 11	3.19±0.06	4.21±0.04
Water with 30%wt of glycerol	4	3.10 ± 0.06	$6.39 \times 10^{-10} \pm 1.3 \times 10^{-11}$	468 ± 7	3.15±0.06	4.49±0.04
	5	3.37 ± 0.08	$6.86 \times 10^{-10} \pm 1.4 \times 10^{-11}$	478 ± 8	3.26±0.07	4.68±0.05
Water with 40%wt of glycerol	6	2.78 ± 0.06	$3.14 \times 10^{-9} \pm 6.4 \times 10^{-11}$	297 ± 4	2.96±0.04	4.17±0.04
Water with 60%wt of glycerol	7	3.52 ± 0.06	$1.42 \times 10^{-7} \pm 3 \times 10^{-9}$	140 ± 2	3.92±0.05	4.52±0.04
	8	4.08 ± 0.09	$1.17 \times 10^{-7} \pm 2 \times 10^{-9}$	158 ± 2	4.24±0.08	4.87±0.05
	9	6.87 ± 0.13	$1.35 \times 10^{-7} \pm 2 \times 10^{-9}$	202 ± 2	5.73±0.07	6.32±0.05
	10	7.98 ± 0.15	$1.30 \times 10^{-7} \pm 2 \times 10^{-9}$	221 ± 2	6.26±0.07	6.81±0.05

Table 1: Characteristics of the ten experiments of Mikaelian et al. (2013). The numbers after ± are the uncertainties of the dimensionless numbers and the measurement error of $< d_e >$.

2.3. Data postprocessing method

The recorded images of the selected experimental set of Mikaelian et al. (2013) are postprocessed using UTHSCSA ImageTool 3.00 (referred hereafter

This is the preprint version of a manuscript published in Experimental Thermal and Fluid Science 64 (2015), p. 1-12.
Permalink: http://dx.doi.org/10.1016/j.expthermflusci.2015.01.013

as IT) and Wolfram Mathematica 7 (referred hereafter as WM7) in order to investigate the three topics described in the introduction. The structure of the postprocessing for a given experiment is presented in Fig. 3 and is detailed in this section.

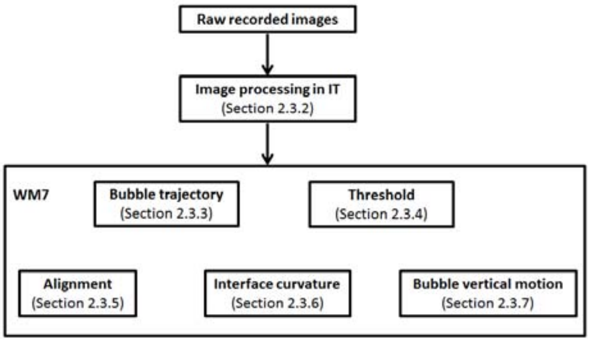

Figure 3: Structure of the postprocessing for a given experiment of the experimental set of Mikaelian et al. (2013).

2.3.1. Definitions

In the ten experiments of Mikaelian et al. (2013), an appropriate approximation of the bubble shape is an ellipsoid with its minor axis as a symmetry axis. The general case of an ellipsoid with a fore-and-aft asymmetry is considered and sketched in Fig. 4 where a is defined as the major axis length of the bubble, b_1 the semi-minor axis length at the front of the bubble and b_2 the semi-minor axis length at the rear of the bubble.

The projection of such an ellipsoidal bubble onto the RPC is an ellipse with a for-and-aft asymmetry, as shown in Fig. 5 where xy is the horizontal plane passing through the bubble mass center, $\vec{v}$ is the velocity vector of the

This is the preprint version of a manuscript published in Experimental Thermal and Fluid Science 64 (2015), p. 1-12.
Permalink: http://dx.doi.org/10.1016/j.expthermflusci.2015.01.013

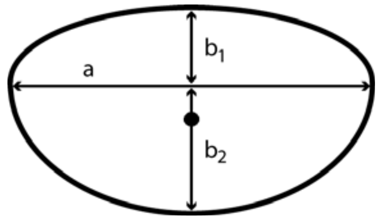

Figure 4: Ellipsoidal shape of a real bubble with a fore-and-aft asymmetry where a is the major axis length of the bubble, b_1 the semi-minor axis length at the front of the bubble, b_2 the semi-minor axis length at the rear of the bubble and $\bullet$ the bubble mass center.

bubble mass center, α is the angle between $\vec{v}$ and the plane xy, $\vec{v}_{\text{proj}}$ is the velocity vector of the bubble projection mass center and α_{proj} is the angle between $\vec{v}_{\text{proj}}$ and the direction y. The angle between the minor axis of the ellipsoidal bubble and the plane xy is named θ and the angle between the minor axis of the bubble projection and the direction y is named θ_{proj}. θ and θ_{proj} are not presented in Fig. 5 for the sake of clarity. As the studied ellipsoidal bubbles have a fore-and-aft asymmetry, the $y - z$ coordinates of the bubble projection mass center are not equal to the $y-z$ coordinates of the projection of the bubble mass center. For the experimental set analyzed in this work, using a code written for WM7, it was verified that the discrepancy between the $y - z$ coordinates of theses two points on the RPC is less than 0.5 pixels. Therefore, it can be supposed that the projection of $\vec{v}$ on the RPC is almost parallel to $\vec{v}_{\text{proj}}$. The orthogonal projection of α on the RPC is thus almost equal to α_{proj}. The orthogonal projection of θ on the RPC is an angle equal to the angle θ_{proj}.

As it is described in the following of this work, α_{proj} is evaluated based on the analysis of the successive positions of the bubble projection mass

This is the preprint version of a manuscript published in Experimental Thermal and Fluid Science 64 (2015), p. 1-12.
Permalink: http://dx.doi.org/10.1016/j.expthermflusci.2015.01.013

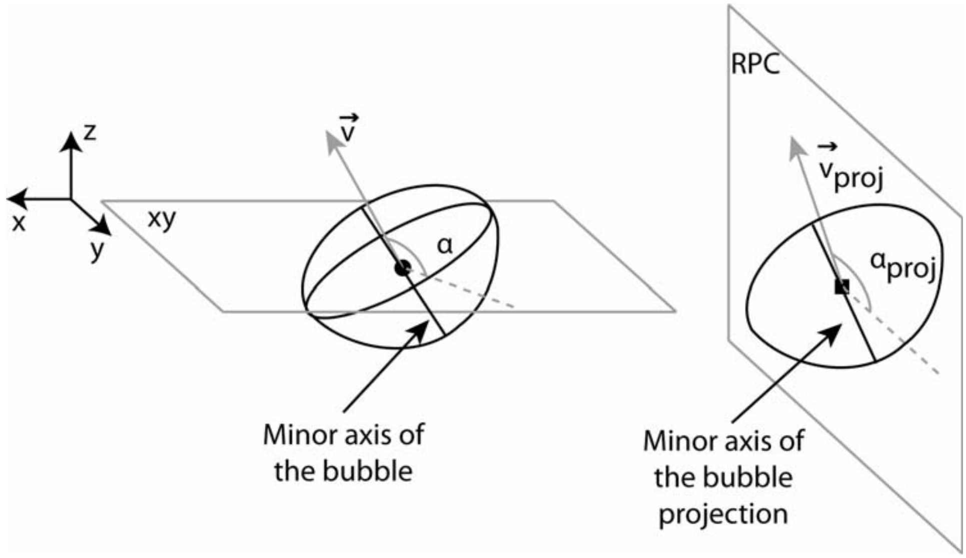

Figure 5: Bubble and its projection onto the RPC with • the bubble mass center, ■ the bubble projection mass center, (x, y, z) the reference frame attached to the bubble mass center, xy the horizontal plane passing through the bubble mass center, $\vec{v}$ the velocity vector of the bubble mass center, α the angle between $\vec{v}$ and the plane xy, $\vec{v}_{\text{proj}}$ the velocity vector of the bubble projection mass center and α_{proj} the angle between $\vec{v}_{\text{proj}}$ and the direction y.

center and θ_{proj} is evaluated based on the analysis of the bubble projection morphology, with the recorded images of the considered bubble.

2.3.2. Image processing in Image Tool

For each experiment, the whole set of recorded images is first processed using a script written for IT. This script comprises the following steps.

1. Binarization of the grayscale images by applying a threshold of 80. The grayscale images are converted to binary images where 0 corresponds to black and 255 to white.
2. Elimination of the empty images. As there is a time interval between

This is the preprint version of a manuscript published in Experimental Thermal and Fluid Science 64 (2015), p. 1-12.
Permalink: http://dx.doi.org/10.1016/j.expthermflusci.2015.01.013

the generations of two successive bubbles, most of the images do not contain any bubble projection. For each bubble of the experiment, the script identifies the images where a bubble is observed and keeps only those images.

3. Evaluation of the mass center coordinates and the minor axis length of the bubble projection for all the images where a bubble is visible. This evaluation is undertaken by using the IT default functions.

The outputs of the image processing in IT are:

- all the raw images containing a bubble projection. These images are grouped based on the bubble number during the experiment;
- for each of these images, the mass center coordinates and the minor axis length of the bubble projection.

The subsequent analysis of the bubble dynamics, realized in WM7 using the bubble projection mass center coordinates determined with IT, appears to be not significantly influenced by the choice of the threshold in IT (80) for the binarization of the images. However, if the binary images generated in IT are used for the analysis of the bubble morphology, it appears that the results of this analysis are significantly influenced by the choice of this threshold. Therefore, the binary images generated in IT are not used in WM7.

2.3.3. Trajectory of a rising bubble

The successive positions of a bubble projection mass center is called hereafter "the bubble projection mass center trajectory". In this work, two types

This is the preprint version of a manuscript published in Experimental Thermal and Fluid Science 64 (2015), p. 1-12.
Permalink: http://dx.doi.org/10.1016/j.expthermflusci.2015.01.013

of trajectories are observed for the rising bubbles: a helix or a zigzag in a vertical plane making an angle ϕ with the RPC. It is here *a priori* assumed that the velocity vector and the minor axis of the bubble are parallel. This assumption is verified in Section 2.3.5. Among all the images recorded during the rise of a bubble, the one where the bubble projection exhibits the smallest minor axis length is selected using the outputs of IT. This image will be referred to in the following as the smallest minor axis length projection (SMALP) image. It is expected that, when such an image is acquired, the bubble minor axis and thus the bubble velocity vector are almost parallel to the RPC. Therefore, it can be seen, that, in the case of a zigzag motion of the bubble, the bubble projection mass center on the SMALP image is located close to an extremum of the bubble projection mass center trajectory (see example in Fig. 6 (b)). In the case of a helical motion of the bubble, the bubble projection mass center on the SMALP image is located close to an inflection point of the bubble projection mass center trajectory (see example in Fig. 6 (a)). A simple technique to identify the type of a bubble trajectory is thus to analyze where the bubble projection mass center on the SMALP image is located on the bubble projection mass center trajectory.

For each bubble of an experiment, the successive coordinates of the mass center of the bubble projection (y_b, z_b) are fitted, using WM7, by the following equation:

$$\vec{Tr} = (R \sin[2\pi\, f_y\, t + \Theta] + K_1 + K_2\, t, K_3 + v\, t) \tag{5}$$

This is the preprint version of a manuscript published in Experimental Thermal and Fluid Science 64 (2015), p. 1-12.
Permalink: http://dx.doi.org/10.1016/j.expthermflusci.2015.01.013

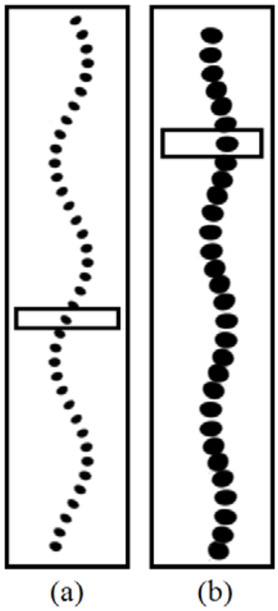

Figure 6: Superposition of some recorded images of the rises of (a) a bubble of Experiment 2; (b) a bubble of Experiment 5. The bubble projections observed on the SMALP images are framed.

where R and f_y are the amplitude and the frequency of a possible oscillation, respectively, v is the vertical velocity of the mass center of the bubble projection and t is the time.

R, f_y, v, Θ, K_1, K_2 and K_3 are unknown parameters which are estimated, for each analyzed bubble, by fitting Eq. 5 to the successive positions of the bubble projection mass center on the RPC. Therefore, these seven parameters might have different values for different bubbles in the same experiment. Eq. 5 can be used to describe the linear, zigzag or helical trajectories. In the case of a helical motion of the bubble, R and f correspond to the amplitude and frequency of this helical motion. It is worth noting that a rise at a constant

This is the preprint version of a manuscript published in Experimental Thermal and Fluid Science 64 (2015), p. 1-12.
Permalink: http://dx.doi.org/10.1016/j.expthermflusci.2015.01.013

vertical velocity v is considered in Eq. 5. It will be shown, in Section 2.3.7, that a weak pulsation can exist in the vertical motion of the bubble.

2.3.4. Threshold for the binarization of the selected images in WM7

In WM7, a technique is developed in order to identify a threshold (λ) for the binarization of the raw images, based on a well-defined criterion. For a given experiment, the steps of this technique are:

1. Five bubbles of the analyzed experiment are randomly selected.
2. The volume V_{bc} of each of the five bubbles is calculated using the following technique:
   (a) Among all the images recorded during the rise of a bubble, the SMALP image is selected. When the SMALP image is acquired, the minor axis of the bubble is almost parallel to the RPC. Therefore, on this image, the length of the minor axis of the bubble projection is equal to the length of the minor axis of the bubble $(b_1 + b_2)$.
   (b) On the SMALP image, a window of 100×100 pixels containing the entire bubble projection is selected and the background is subtracted for this window.
   (c) This new image is binarized using a first estimation of the threshold λ.
   (d) The contour of the bubble projection is determined.
   (e) The points of the contour are sorted. An arbitrary starting point on the contour is chosen. The $(i+1)^{\text{th}}$ point on the contour is

This is the preprint version of a manuscript published in Experimental Thermal and Fluid Science 64 (2015), p. 1-12.
Permalink: http://dx.doi.org/10.1016/j.expthermflusci.2015.01.013

chosen as being the closest point to the i^{th} point that is not the $(i-1)^{\text{th}}$ point.

(f) The contour is smoothed by replacing each point of the contour by a new one located at the middle of the line segment joining this point and the following one on the contour. This smoothing technique is iterated four times.

(g) The smoothed contour is fitted, using the least square method *Fit* in WM7, by two half ellipses (one at the front and another at the rear of the bubble) having the same center and the same major axis. The fitting parameters are the center coordinates, the minor axis lengths of the two half ellipses, the major axis length of the two half ellipses and the angle between the major axis and the horizontal direction. As the SMALP image is considered, this major axis length, the semi-minor axis length of the front half ellipse and the semi-minor axis length of the rear half ellipse are equal to a, b_1 and b_2, respectively.

(h) The volume of the bubble V_{bc} is then calculated by $V_{bc} = \frac{\pi a^2 b_1}{6} + \frac{\pi a^2 b_2}{6}$.

3. An average volume $< V_{bc} >$ is calculated for the five selected bubbles.
4. The value of the threshold used in Step 2c is adjusted by dichotomy and the steps from 2c to 3 are iterated until $< V_{bc} >$ is close by less than 1.5% to V_b (obtained experimentally with the bubble collector as described in Section 2.2).

This is the preprint version of a manuscript published in Experimental Thermal and Fluid Science 64 (2015), p. 1-12.
Permalink: http://dx.doi.org/10.1016/j.expthermflusci.2015.01.013

Some steps of the technique described above are presented in Fig. 7.

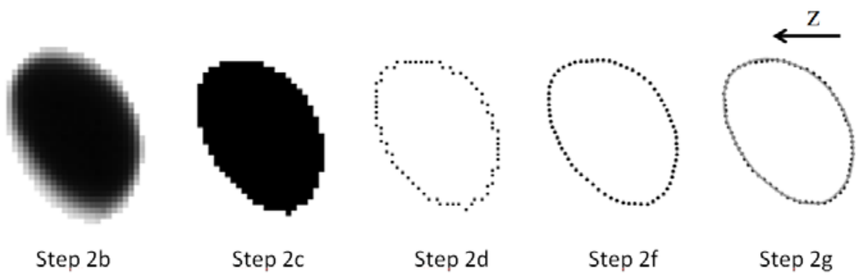

Figure 7: Examples of the steps 2b, 2c, 2d, 2f and 2g of the technique in Section 2.3.4 for a bubble of Experiment 2.

2.3.5. Alignment of the minor axis and the velocity vector of a bubble

The possible alignment of the minor axis and the velocity vector of a bubble rising in liquid can be analyzed using two complementary approaches. In the first approach, this alignment is analyzed using all the recorded images of one bubble randomly selected among all the bubbles of an experiment. In the second approach, this alignment is analyzed using one specific image (the SMALP image) for all of the bubbles of an experiment.

The first approach consists in comparing the projections, on the RPC, of the bubble minor axis and the bubble velocity vector, for all the recorded images of one bubble randomly selected from all the bubbles of an experiment. As explained in Section 2.3.1, the projection on the RPC of the bubble minor axis is parallel to the bubble projection minor axis and the projection on the RPC of the bubble velocity vector is almost parallel to the bubble projection velocity vector. Therefore, the projection on the RPC of the bubble minor

This is the preprint version of a manuscript published in Experimental Thermal and Fluid Science 64 (2015), p. 1-12.
Permalink: http://dx.doi.org/10.1016/j.expthermflusci.2015.01.013

axis and the projection on the RPC of the bubble velocity vector can be characterized by θ_{proj} and α_{proj}, respectively.

The angle θ_{proj} is evaluated for a recorded bubble projection by analyzing its morphology thanks to the following technique written for WM7.

1. A window of 100×100 pixels containing the entire bubble projection is selected and the background is subtracted for this window.
2. The bubble projection is binarized using the threshold λ determined in Section 2.3.4, for the considered experiment.
3. The contour of the bubble projection is determined.
4. The contour of the bubble consists of N points. Each point i of the contour is associated to the $N-1$ other points of the contour to generate the line segments l_{ij} with $i = 1, 2, ..., N$ and $j = 1, 2, ..., i-1, i+1, ..., N$ (see Fig. 8). For each line segment l_{ij}, its length L_{ij} and the angle β_{ij} between it and the y direction are calculated. The angles, expressed in degrees (°) are rounded at the closest integer.
5. An angle ξ is varied between 0° and 180° by steps of 1°. For each ξ, the longest line segment l_{ij}, such that $\beta_{ij} = \xi$, is identified. Its length is written $L_{\max}(\xi)$. An array $(\xi, L_{\max}(\xi))$ is then built. The first and the last 30 elements of this array are dropped in order to keep only elements with a value of $L_{\max}$ close to its minimum (see Fig. 8). A third-order polynomial fit is computed for $L_{\max}$ versus ξ (see Fig. 8). The abscissa of the minimum of this function is θ_{proj}.

It is important to highlight that this technique for the identification of

This is the preprint version of a manuscript published in Experimental Thermal and Fluid Science 64 (2015), p. 1-12.
Permalink: http://dx.doi.org/10.1016/j.expthermflusci.2015.01.013

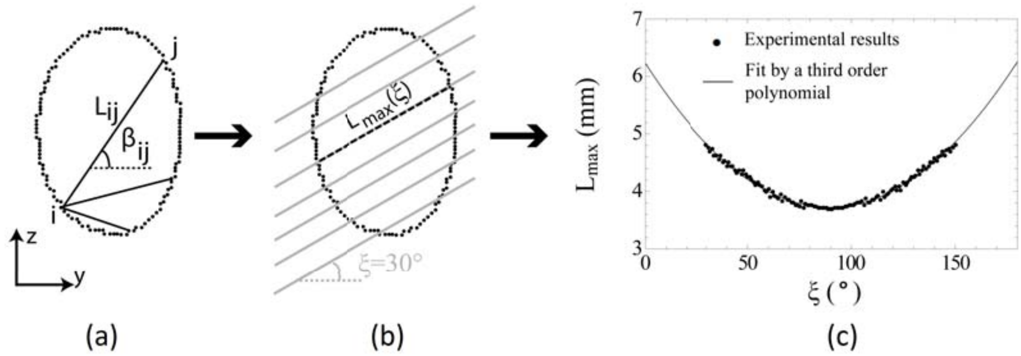

Figure 8: Example for Experiment 5 of (a) the generation of line segments by linking the point i of the contour to other points of the contour; (b) the determination of $L_{\max}$ for $\xi = 30°$; (c) the fit of the experimental results $(\xi, L_{\max})$ by a third-order polynomial.

θ_{proj} does not require to assume that the bubble projection is composed of two ellipses (unlike in the technique used for the determination of the threshold for the binarization of the raw images). It appears thus to be more general.

The angle α_{proj} is evaluated for a recorded bubble projection using the mass center coordinates (y_{b1}, z_{b1}) of this projection and the mass center coordinates of the next recorded bubble projection (y_{b2}, z_{b2}):

$$\alpha_{\text{proj}} = \tan^{-1} \frac{z_{b2} - z_{b1}}{y_{b2} - y_{b1}} \tag{6}$$

For the selected bubble, θ_{proj} and α_{proj} are calculated for every two recorded projections of this bubble. The alignment of the minor axis and the velocity vector of the bubble is validated (or not) by evaluating the deviation $s_{\text{all images}}$ between θ_{proj} and α_{proj} by:

This is the preprint version of a manuscript published in Experimental Thermal and Fluid Science 64 (2015), p. 1-12.
Permalink: http://dx.doi.org/10.1016/j.expthermflusci.2015.01.013

$$s_{\text{all images}} = \sqrt{\sum_{\text{all analyzed images}} \frac{(\theta_{\text{proj}} - \alpha_{\text{proj}})^2}{(\alpha_{\text{proj}})^2 n}} \tag{7}$$

where n is the number of analyzed projections of the considered bubble.

The second approach is a specific case of the first approach where only SMALP images are considered. When a SMALP image is recorded, the bubble minor axis is almost parallel to the bubble projection minor axis and, thus θ is almost equal to θ_{proj} and α to α_{proj}. Therefore, the alignment of the minor axis and the velocity vector of a bubble is fully investigated in this second approach. In the first approach, the alignment of the minor axis and the velocity vector of a bubble is only partially characterized, as it is the projections on the RPC of these two vectors that are considered and compared. The angles θ_{proj} and α_{proj} of a bubble projection on a SMALP image are referred to hereafter as θ_S and α_S, respectively. For each of the bubbles of the selected experiment, θ_S and α_S are evaluated by calculating θ_{proj} and α_{proj} for the bubble projection on the SMALP image as described above. The alignment of the minor axis and the velocity vector of the bubbles of the selected experiment is validated (or not) by evaluating the deviation s_{SMALP} by:

$$s_{\text{SMALP}} = \sqrt{\sum_{\text{all analyzed bubbles}} \frac{(\theta_S - \alpha_S)^2}{(\alpha_S)^2 n_b}} \tag{8}$$

where n_b is the number of analyzed bubbles in the considered experiment.

This is the preprint version of a manuscript published in Experimental Thermal and Fluid Science 64 (2015), p. 1-12.
Permalink: http://dx.doi.org/10.1016/j.expthermflusci.2015.01.013

2.3.6. Interface curvature radii at the front and at the rear of a bubble

For each bubble of a considered experiment, the interface curvature radii at the front r_f and at the rear r_r of the bubble are evaluated using the following technique (which is similar to the one used in Section 2.3.4).

1. Among all the images recorded during the rise of a bubble, the SMALP image is identified.
2. A window of 100×100 pixels containing the entire bubble projection is selected and the background is subtracted for this window.
3. This new image is binarized using the threshold λ determined in Section 2.3.4, for the considered experiment.
4. The contour of the bubble projection is determined.
5. The points of the contour are sorted and the contour is smoothed as described in Section 2.3.4.
6. The smoothed contour is fitted by two half ellipses (one for the front and another for the rear of the bubble) with the same center and the same major axis, as described in Section 2.3.4. As the SMALP image is considered, this major axis length, the semi-minor axis length of the front half ellipse and the semi-minor axis length of the rear half ellipse are equal to a, b_1 and b_2, respectively.
7. r_f and r_r are calculated by $r_f = a^2/4b_1$ and $r_r = a^2/4b_2$.

r_f and r_r are evaluated for all the bubbles of the considered experiment and the mean values (R_f and R_r) and the standard deviations (σ_{r_f} and

This is the preprint version of a manuscript published in Experimental Thermal and Fluid Science 64 (2015), p. 1-12.
Permalink: http://dx.doi.org/10.1016/j.expthermflusci.2015.01.013

σ_{r_r}) are then deduced. The ratio $\frac{R_f}{R_r}$ and its uncertainty $\Delta(R_f/R_r)$ are also evaluated.

2.3.7. Pulsation in the dynamics of the vertical motion of the bubble mass center

For each bubble of a considered experiment, $z_{rel} = z_b - v\,t$ is evaluated, with v identified as presented in Section 2.2. z_{rel} is the difference between the vertical position of the bubble mass center z_b and the position $v\,t$ where it would have been if the bubble was rising at a constant vertical velocity v.

The power spectral density of z_{rel} is computed using the discrete Fourier transform function in WM7. If a strong peak can be identified in this power spectral density, it is used to determine a characteristic frequency f_z in the vertical motion of the bubble mass center. f_z is then normalized by f_y (see Eq. 5). $F_z = f_z/f_y$ is evaluated for all the bubbles of the considered experiment and a mean value $< F_z >$ and a standard deviation σ_{F_z} are then deduced.

3. Results and discussion

3.1. Trajectory of the rising bubbles

For the ten experiments presented in Tab. 1, the type of the bubble trajectory is determined using the technique described in Section 2.3.3. The results are presented in Tab. 2.

This is the preprint version of a manuscript published in Experimental Thermal and Fluid Science 64 (2015), p. 1-12.
Permalink: http://dx.doi.org/10.1016/j.expthermflusci.2015.01.013

Exp.	Type of the bubble trajectory
1 2 3	helical motion
4 5 6 7 8 9 10	zigzag motion

Table 2: Type of the bubble trajectory.

3.2. Alignment of the minor axis and the velocity vector of a bubble

In the first approach, for each of the ten experiments presented in Tab. 1, θ_{proj} and α_{proj} are evaluated for every two projections of a randomly selected bubble, as described in Section 2.3.5. $s_{\text{all images}}$ is then evaluated for this bubble.

In Figs. 9 and 10, two typical results are shown where the time evolutions of θ_{proj} and α_{proj} (a) and y_b (b) are presented for a randomly selected bubble of Experiments 1 and 5, respectively. These two experiments were chosen because a helical motion of the bubble is observed in Experiment 1 and a zigzag motion of the bubble is observed in Experiment 5 (see Tab. 2).

This is the preprint version of a manuscript published in Experimental Thermal and Fluid Science 64 (2015), p. 1-12.
Permalink: http://dx.doi.org/10.1016/j.expthermflusci.2015.01.013

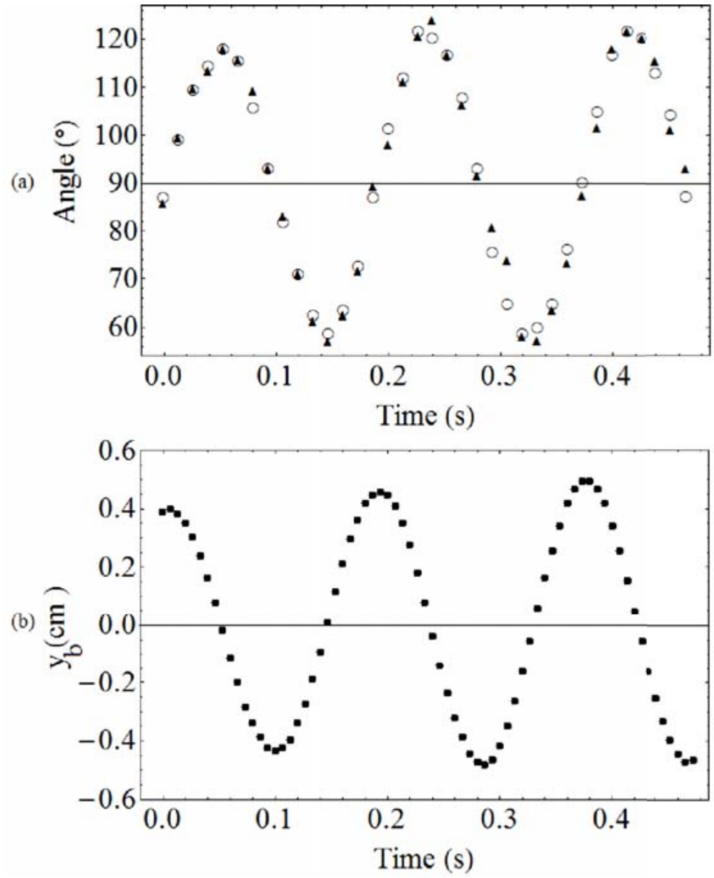

Figure 9: (a) θ_{proj} (▲) and α_{proj} (∘) and (b) y_b as functions of the time for a helical motion of a bubble (Experiment 1 of Tab. 1).

This is the preprint version of a manuscript published in Experimental Thermal and Fluid Science 64 (2015), p. 1-12.
Permalink: http://dx.doi.org/10.1016/j.expthermflusci.2015.01.013

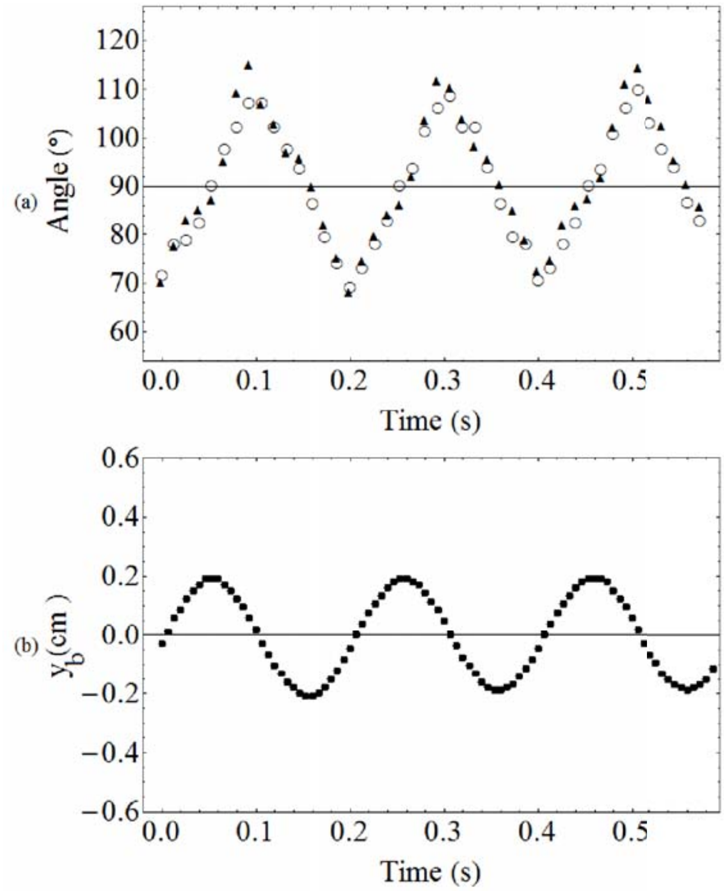

Figure 10: (a) θ_{proj} (▲) and α_{proj} (○) and (b) y_b as functions of the time for a zigzag motion of a bubble (Experiment 5 of Tab. 1).

The values of $s_{\text{all images}}$ for all the experiments of Tab. 1 are presented in Tab. 3. $s_{\text{all images}}$ is lower than 10% for all the experiments, except for Experiment 10.

This is the preprint version of a manuscript published in Experimental Thermal and Fluid Science 64 (2015), p. 1-12.
Permalink: http://dx.doi.org/10.1016/j.expthermflusci.2015.01.013

Exp.	$s_{\text{all images}}$ (%)
1	3.5
2	4.3
3	7.5
4	5.0
5	3.6
6	2.3
7	5.1
8	5.5
9	9.9
10	14.1

Table 3: $s_{\text{all images}}$ evaluated for all the experiments of Tab. 1.

In the second approach, for each of the ten experiments presented in Tab. 1, θ_S and α_S are calculated for all the bubbles of the experiment, as described in Section 2.3.5. As well as s_{SMALP}, the mean values $< \theta_S >$ and $< \alpha_S >$ and the standard deviations σ_{θ_S} and σ_{α_S} of θ_S and α_S are evaluated for each experiment. The results are presented in Tab. 4.

Exp.	$< \theta_S >$ (°)	σ_{θ_S} (°)	$< \alpha_S >$ (°)	σ_{α_S} (°)	s_{SMALP} (%)
1	61.3	3.6	62.3	3.4	2.8
2	58.5	1.9	62.1	1.6	6.6
3	60.7	1.9	64.9	1.8	7.1
4	90.5	2.4	90.5	4.5	4.9
5	89.9	2.0	89.9	4.1	4.3
6	91.0	1.4	90.9	1.9	2.9
7	90.7	2.2	89.7	3.2	3.2
8	89.2	4.2	87.9	3.8	4.5
9	90.4	1.4	88.7	7.1	8.3
10	91.3	1.9	85.3	8.7	13.1

Table 4: $< \theta_S >$, σ_{θ_S}, $< \alpha_S >$, σ_{α_S} and s_{SMALP} evaluated for all the experiments of Tab. 1.

This is the preprint version of a manuscript published in Experimental Thermal and Fluid Science 64 (2015), p. 1-12.
Permalink: http://dx.doi.org/10.1016/j.expthermflusci.2015.01.013

Two different trends are visible in Tab. 4 between the case of a zigzag motion and the case of a helical motion of the bubbles. Indeed, $< \theta_S >$ and $< \alpha_S >$ are close to 90° in the case of a zigzag motion of the bubbles and close to 60° in the case of a helical motion of the bubbles. The value of 90° for α_S in the case of a zigzag motion of the bubble was expected. The value of 60° for α_S in the case of a helical motion of the bubble is in agreement with results in the literature (Mougin and Magnaudet (2002), Shew et al. (2006)). It is also observed, in Tab. 4, that, for an helical motion of a bubble, the values of $< \theta_S >$ and $< \alpha_S >$ are almost independent of the bubble size and of the water-glycerol mixture used.

The alignment of the minor axis and the velocity vector of a bubble can be assessed in the case of a zigzag motion and in the case of a helical motion of the bubble. Indeed:

- θ_{proj} and α_{proj} have values close to each other for all the analyzed projections in Figs. 9 and 10;

- except for the Experiment 10, it is shown in Tab. 3 that $s_{\text{all images}}$ is lower than 10% for all the experiments of Tab. 1;

- it is shown in Tab. 4, that $< \theta_S >$ and $< \alpha_S >$ have values close to each other and that s_{SMALP} is lower than 10% for all the experiments of Tab. 1, except for the Experiment 10.

The alignment between the minor axis and the velocity vector of a bubble observed here is in agreement with the works of Saffman (1956) and Ellingsen

This is the preprint version of a manuscript published in Experimental Thermal and Fluid Science 64 (2015), p. 1-12.
Permalink: http://dx.doi.org/10.1016/j.expthermflusci.2015.01.013

and Risso (2001). The way this alignment is assessed here is different than in these works. Indeed, the directions of the minor axis and of the velocity vector of a bubble are here directly determined from experimental results and then compared to analyze their alignment, for the successive positions of the bubble.

3.3. Interface curvature radii at the front and at the rear of a bubble

For all the experiments of Tab. 1, R_f, R_r, σ_{r_f}, σ_{r_r}, R_f/R_r and $\Delta(R_f/R_r)$ are evaluated, as described in Section 2.3.6. The results are presented in Tab. 5.

Exp.	R_f (mm)	σ_{r_f} (mm)	R_r (mm)	σ_{r_r} (mm)	R_f/R_r	$\Delta(R_f/R_r)$
1	4.32	0.40	2.66	0.14	1.62	0.29
2	2.53	0.11	1.80	0.08	1.41	0.13
3	6.13	0.51	3.98	0.28	1.54	0.27
4	3.88	0.10	3.21	0.04	1.21	0.04
5	4.18	0.08	3.43	0.05	1.22	0.04
6	3.35	0.09	2.96	0.07	1.13	0.06
7	3.68	0.07	3.44	0.03	1.07	0.03
8	4.25	0.08	3.90	0.07	1.09	0.04
9	7.41	0.15	6.20	0.16	1.19	0.05
10	8.64	0.47	7.15	0.15	1.21	0.10

Table 5: R_f, σ_{r_f}, R_r, σ_{r_r}, R_f/R_r and $\Delta(R_f/R_r)$ evaluated for all the experiments of Tab. 1.

The results presented in Tab. 5 show that the ratio R_f/R_r can reach up to 1.62. The fore-and-aft asymmetry can thus be substantial. For the values of Eo and Mo considered in this work (see Tab. 1), R_f is higher than R_r, meaning that the interface at the front of the bubble is flatter than at the

This is the preprint version of a manuscript published in Experimental Thermal and Fluid Science 64 (2015), p. 1-12.
Permalink: http://dx.doi.org/10.1016/j.expthermflusci.2015.01.013

rear. This observation is in agreement with the results of Ryskin and Leal (1984), Duineveld (1995) and Zenit and Magnaudet (2008).

By cross analyzing the data of Tab. 5 and Tab. 1, it can be observed that R_f/R_r increases when Mo decreases and when Eo as well as We increase. This could be explained by the fact that, at low Mo and high Eo and We, viscous and surface tension forces are dominated by inertial forces. The inertial forces tend to flatten the bubble interface and they do it in an asymmetric way between the front and the rear of the bubble because the flow field is different in these two regions.

The results in Tab. 5 can be classified in two groups: one where an helical motion of a bubble with a high value of R_f/R_r is observed (Experiments 1 to 3 of Tab. 1) and another where a zigzag motion of a bubble with a lower value of R_f/R_r is observed (Experiments 4 to 10 of Tab. 1). The second group is characterized by $3 < \mathrm{Eo} < 8$ and $6 \times 10^{-10} < \mathrm{Mo} < 10^{-7}$ (water-glycerol mixtures with more than 30%wt glycerol). For this group, based on the forms of the correlations presented by Mikaelian et al. (2013), the following expression is proposed for R_f/R_r as a function of Eo and Mo:

$$\frac{R_f}{R_r} = k_1\, \mathrm{Eo}^{k_2} \mathrm{Mo}^{k_3} \tag{9}$$

where k_1, k_2 and k_3 are fitting parameters.

Eq. 9 is fitted to the experimental data of R_f/R_r by adjusting k_1, k_2 and

This is the preprint version of a manuscript published in Experimental Thermal and Fluid Science 64 (2015), p. 1-12.
Permalink: http://dx.doi.org/10.1016/j.expthermflusci.2015.01.013

k_3. It leads to the correlation:

$$\frac{R_f}{R_r} = 0.555\,\mathrm{Eo}^{1/6}\mathrm{Mo}^{-1/36} \tag{10}$$

The values of R_f/R_r computed by Eq. 10 are successfully compared to the experimental values of R_f/R_r in Fig. 11. For given liquid properties and bubble size characterized by $3 < \mathrm{Eo} < 8$ and $6 \times 10^{-10} < \mathrm{Mo} < 10^{-7}$, Eq. 10 enables an estimation of R_f/R_r. This estimation can be used in order to reconstruct the shape of a bubble knowing its deformation χ, defined as $\frac{b_1+b_2}{a}$, and its equivalent diameter d_e. A correlation for the deformation χ of a bubble as a function of its Eo and Mo has been proposed in Mikaelian et al. (2013) for $3 < \mathrm{Eo} < 8$ and $6 \times 10^{-10} < \mathrm{Mo} < 10^{-7}$.

This is the preprint version of a manuscript published in Experimental Thermal and Fluid Science 64 (2015), p. 1-12.
Permalink: http://dx.doi.org/10.1016/j.expthermflusci.2015.01.013

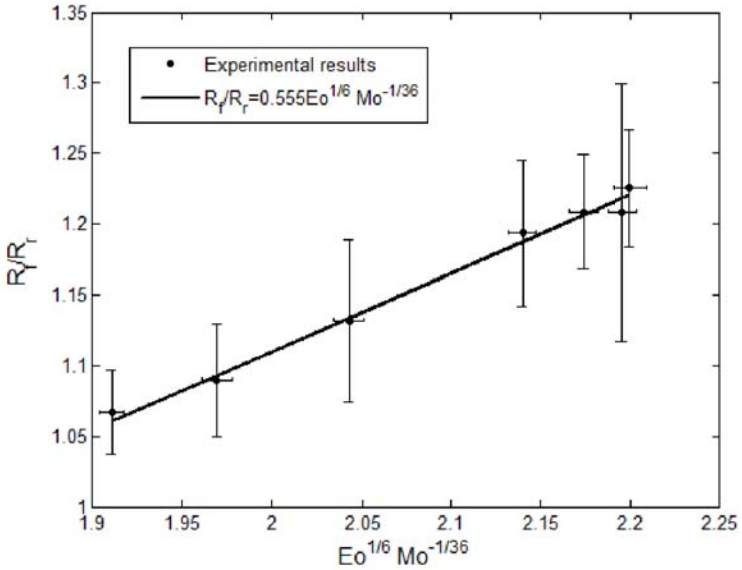

Figure 11: Comparison between the values of R_f/R_r computed by Eq. 10 and the experimental results.

In the case of a zigzag motion of a bubble, a correlation is obtained for R_f/R_r as a function of the Eo and Mo of the bubble (see Eq. 10). It could be interesting to carry out new experiments where an helical motion of the generated bubbles is observed. The amount of available experiments will then be large enough to develop, in the case of a helical motion of a bubble, a (possible) correlation for R_f/R_r as a function of the Eo and Mo of the bubble.

This is the preprint version of a manuscript published in Experimental Thermal and Fluid Science 64 (2015), p. 1-12.
Permalink: http://dx.doi.org/10.1016/j.expthermflusci.2015.01.013

3.4. Pulsation in the dynamics of the vertical motion of the bubble mass center

For each of the ten experiments presented in Tab. 1, z_{rel} and its power spectral density are calculated for each bubble of the experiment, as described in Section 2.3.7.

The time evolutions of z_{rel} and y_b, and the power spectral density of z_{rel} are presented for a randomly selected bubble of Experiment 5 (zigzag motion) in Figs. 12 and 13 and for a randomly selected bubble of Experiment 3 (helical motion) in Figs. 12 and 13.

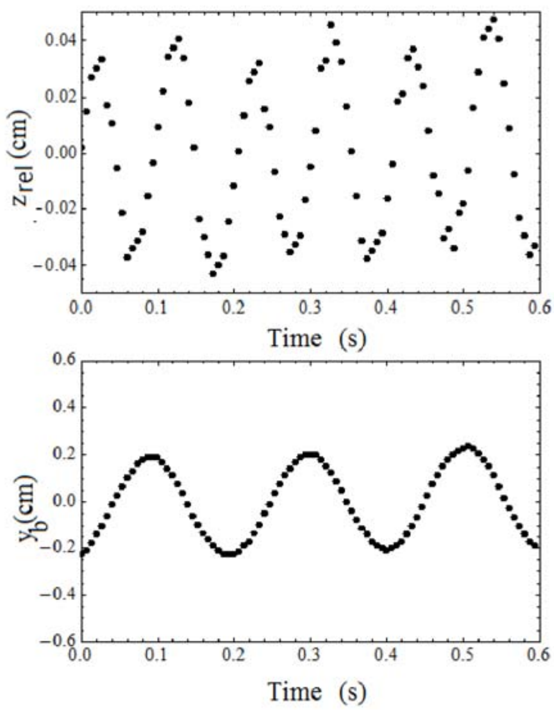

Figure 12: (a) z_{rel} and (b) y_b as functions of the time for a zigzag motion of a bubble (Experiment 5 of Tab. 1).

This is the preprint version of a manuscript published in Experimental Thermal and Fluid Science 64 (2015), p. 1-12.
Permalink: http://dx.doi.org/10.1016/j.expthermflusci.2015.01.013

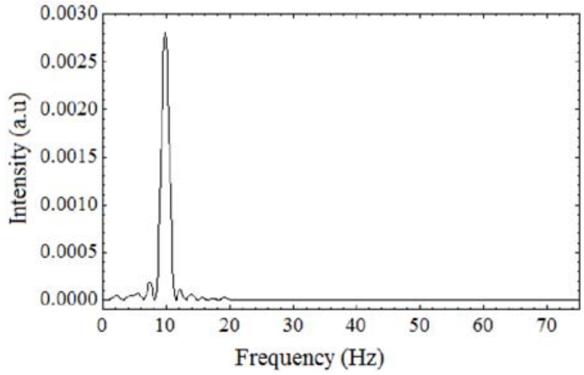

Figure 13: Power spectral density of z_{rel} for the bubble of Fig. 12.

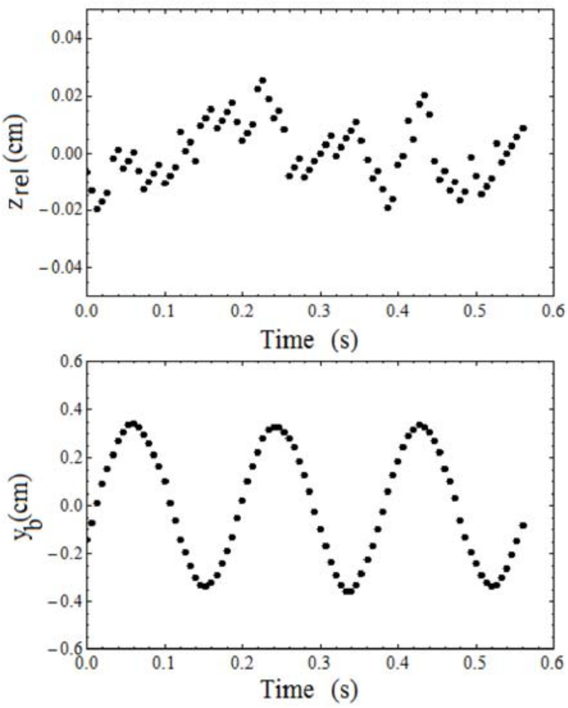

Figure 14: (a) z_{rel} and (b) y_b as functions of the time for a helical motion of a bubble (Experiment 3 of Tab. 1).

This is the preprint version of a manuscript published in Experimental Thermal and Fluid Science 64 (2015), p. 1-12.
Permalink: http://dx.doi.org/10.1016/j.expthermflusci.2015.01.013

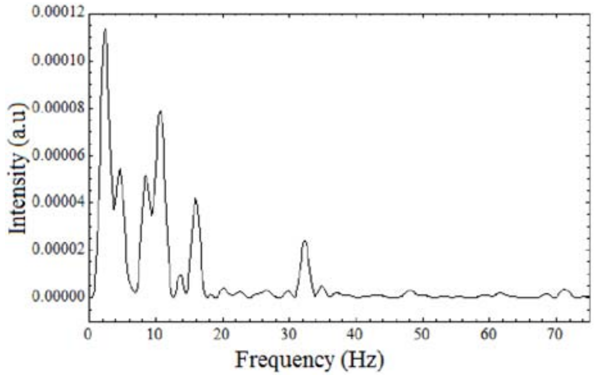

Figure 15: Power spectral density of z_{rel} for the bubble of Fig. 14.

In Fig. 12, a pulsation can be observed in the plot of z_{rel} versus t. The frequency of this pulsation seems approximately twice the frequency of the pulsation in the plot of y_b versus t. The pulsation observed in Fig. 12 is confirmed by the strong peak in the power spectral density of z_{rel} presented in Fig. 13. This peak enables $f_z = 9.8$ Hz to be determined. As the plot of z_{rel} versus t presents a sinusoidal shape, the bubble accelerates along the vertical direction when z_{rel} is negative (approximately between an inflection point and the next extremum of y_b versus t) and accelerates along the vertical direction when z_{rel} is positive (approximately between an extremum and the next inflection point of y_b versus t). The bubble undergoes thus a positive vertical force just after the inflection point of y_b versus t and it undergoes a negative vertical force just after the extrema of y_b versus t. These observations are in agreement with the results of Shew et al. (2006).

In Fig. 14, a pulsation cannot be distinguished in the curve z_{rel} versus t. This suggests that the vertical position of the bubble mass center is changing

This is the preprint version of a manuscript published in Experimental Thermal and Fluid Science 64 (2015), p. 1-12.
Permalink: http://dx.doi.org/10.1016/j.expthermflusci.2015.01.013

randomly around the position $v\,t$ where it would have been if the bubble was rising at a constant vertical velocity v. In the power spectral density of z_{rel} (Fig. 15), peaks of an order of magnitude weaker than the peak in Fig. 13 and distributed irregularly are observed. It confirms the absence of a well defined pulsation in the curve z_{rel} versus t.

For each experiment of Tab. 1, $< F_z >$ and σ_{F_z} are evaluated as described in Section 2.3.7. The results are presented in Tab. 6.

Exp.	$< F_z >$	σ_{F_z}
1	2.25	0.04
2	/	/
3	/	/
4	2.04	0.02
5	2.03	0.02
6	2.03	0.01
7	2.04	0.02
8	2.03	0.03
9	2.08	0.08
10	2.05	0.02

Table 6: $< F_z >$ and σ_{F_z} evaluated for all the experiments of Tab. 1.

In Tab. 6, two distinct groups can be identified: one where F_z is approximately equal to 2 and another where F_z cannot be identified or is not an integer value. The first group corresponds to a zigzag motion of the bubble and the second to a helical motion of the bubble (see Tab. 2). Therefore, it can be suggested that,

- in the case of the zigzag motion of a bubble, a pulsation in the vertical motion of the bubble mass center can be observed with a frequency

This is the preprint version of a manuscript published in Experimental Thermal and Fluid Science 64 (2015), p. 1-12.
Permalink: http://dx.doi.org/10.1016/j.expthermflusci.2015.01.013

twice the frequency of the zigzag motion ($F_z = 2$). This observation is in agreement with the experimental results of Ellingsen and Risso (2001) and Shew et al. (2006).

- in the case of the helical motion of a bubble, no pulsation in the vertical motion of the bubble mass center can be observed with F_z equal to an integer value. This is also observed in the experimental results of Shew et al. (2006).

The two different trends observed above can be explained by the different bubble wake structures in the case of the zigzag and helical motions of the bubbles. These bubble wake structures were investigated by Lunde and Perkins (1997), Brüker (1999), de Vries et al. (2002) and Mougin and Magnaudet (2006). In the case of a zigzag motion of a bubble, a periodic change in the wake of the bubble at twice the frequency f_y is observed in all of these works. This periodic change could then be the origin of the pulsation in the vertical motion of the bubble mass center in the case of a zigzag motion. In the case of a helical motion of the bubble, it was observed by Lunde and Perkins (1997), Brüker (1999) and Mougin and Magnaudet (2006) that the wake is approximately steady in a reference frame attached to the bubble. In such a situation, the vertical force exerted on the bubble due to the wake is almost steady. Therefore, no pulsation in the vertical motion of the bubble mass center is expected.

The evaluation of F_z can be used in order to distinguish the zigzag and the

This is the preprint version of a manuscript published in Experimental Thermal and Fluid Science 64 (2015), p. 1-12.
Permalink: http://dx.doi.org/10.1016/j.expthermflusci.2015.01.013

helical motion of a bubble and leads to the same results as the one presented in Tab. 2. This technique is interesting compared to the technique, based on the SMALP image, described in Section 2.3.3, because it only needs the successive values of the z_b coordinate of a bubble projection mass center to determine the type of its trajectory.

As can be seen in Figs. 12 and 14, values of z_{rel} lower than 0.01 cm can be detected using the experimental set-up and postprocessing method of this work. The precision in the evaluation of the bubble mass center vertical coordinate is thus high. The main sources of errors are the digitizing error, the binarization in IT and the fact that the mass center coordinates of a bubble projection are not equal to the coordinates of the projection onto the RPC of the mass center of the real bubble. The error due to the third source can reach up to 0.5 pixels (equal to 0.005 cm) as explained in Section 2.3.1. The digitizing error is estimated using the work of Ho (1983) and seems negligible compared to the third source of error. For a given experiment, the recorded bubble projections have a quite similar shape. It can then be assumed that the second and third sources of errors only introduce a constant shift in the evaluation of the bubble mass center coordinates. Therefore, the analysis of the dynamics of the bubbles is almost not impacted by these two sources of error and the precision for this analysis is high.

This is the preprint version of a manuscript published in Experimental Thermal and Fluid Science 64 (2015), p. 1-12.
Permalink: http://dx.doi.org/10.1016/j.expthermflusci.2015.01.013

4. Conclusions and perspectives

In this work, an innovative postprocessing method of raw images recorded using the experimental set-up presented in Mikaelian et al. (2013) is developed. It enables the accurate analysis of the dynamics and the morphology of a bubble rising in a liquid. The key points of this postprocessing method are:

- the use of the SMALP image, acquired when the minor axis of the bubble is almost parallel to the recording plane of the camera, for the analysis of the bubble morphology;
- the determination of a threshold λ for the binarization of the images, based on a well defined criterion (volume conservation);
- the use of a technique for the determination of the bubble orientation (θ_{proj}) that does not require to postulate *a priori* a shape of the bubble.

Two techniques are also presented in order to identify the type of the trajectory of a bubble:

- one based on the position of the bubble projection mass center along the bubble projection mass center trajectory when the SMALP image is acquired;
- one based on the detection of a pulsation in the vertical motion of the bubble.

This is the preprint version of a manuscript published in Experimental Thermal and Fluid Science 64 (2015), p. 1-12.
Permalink: http://dx.doi.org/10.1016/j.expthermflusci.2015.01.013

Such an identification is a key point in the analysis of the dynamics of a bubble and is difficult when a single camera is used.

The data postprocessing method is applied on raw images of a subset of the whole experimental set presented in Mikaelian et al. (2013). The experiments considered are those where single ellipsoidal bubbles with an oscillatory trajectory and without interface wobbling are observed. For all the selected experiments, the alignment of the minor axis and the velocity vector of the bubbles is observed as well in the case of a zigzag motion than in the case of a helical motion of the bubble. This is achieved by determining the directions of the minor axis and the velocity vector of the bubble and comparing them. For all the selected experiments, R_f and R_r are evaluated and, in the case of a zigzag motion of a bubble, a correlation for the ratio R_f/R_r is established as a function of its Eo and Mo. In the vertical motion of the bubbles, a pulsation at twice the frequency of the horizontal motion is identified in the case of a zigzag motion of the bubbles. In the case of a helical motion of the bubbles, such a pulsation can not be identified.

As a perspective, the data postprocessing method proposed in this paper can also be applied to ellipsoidal bubble swarms or chains. The type of the bubble trajectory, the possible alignment between the minor axis and the velocity vector of the bubbles, the bubble morphology, and the dynamics of the vertical motion of the bubbles can then be investigated for these bubble swarms and the results can be compared to the cases of single ellipsoidal bubbles.

This is the preprint version of a manuscript published in Experimental Thermal and Fluid Science 64 (2015), p. 1-12.
Permalink: http://dx.doi.org/10.1016/j.expthermflusci.2015.01.013

From the values of R_f and R_r, the shape of a bubble can be reconstructed. This shape could, coupled with the parameters of the bubble trajectory (obtained using Eq. 5) and based on the alignment of its minor axis and its velocity vector, be used to carry out numerical simulations of the flow and the mass transport around these bubbles. For this purpose, the continuity, Navier-Stokes and mass transport equations and the associated boundary conditions could be written in a reference frame attached to the bubble mass center and then solved numerically.

New experiments can be carried out using the experimental set-up presented in Mikaelian et al. (2013) in order to generate ellipsoidal bubbles rising in the liquid with a helical motion and without interface wobbling. These experiments can be postprocessed in order to establish a correlation for R_f/R_r as a function of Eo and Mo in the case of a helical motion of the bubbles.

Acknowledgements

The authors acknowledge Solvay s.a., le Fonds Van Buuren and le Fonds de la Recherche Scientifique (F.R.S.-F.N.R.S.) for their financial contribution.

References

O. Miyagi, Phil. Mag. (6th Series), 50, 112 (1925).

This is the preprint version of a manuscript published in Experimental Thermal and Fluid Science 64 (2015), p. 1-12.
Permalink: http://dx.doi.org/10.1016/j.expthermflusci.2015.01.013

B. Rosenberg, The drag and shape of air bubbles moving in liquids, David W. Taylor Model Basin, Report 727 (1950).

W.L. Haberman & R.K. Morton, An experimental investigation of the drag and shape of air bubbles rising in various liquids, David Taylor Model Basin, Report 802 (1953).

P.G. Saffman, On the rise of small air bubbles in water, J. Fluid Mech. 1, 249-275 (1956).

R.A. Hartunian & W.R. Sears, On the instability of small gas bubbles moving uniformly in various liquids, J. Fluid Mech., 3,27-47 (1957).

D. W. Moore, The rise of a gas bubble in a viscous liquid, J. Fluid Mech., 6, 113-130 (1958).

D. W. Moore, The boundary layer on a spherical gas bubble, J. Fluid Mech., 16, 161-76 (1963).

D. W. Moore, The velocity of rise of distorted gas bubbles in a liquid of small viscosity, J. Fluid Mech., 23, 749-766 (1965).

N.M. Aybers & A. Tapucu, The motion of gas bubbles rising through a stagnant liquid, Wärme- und Stoffübertragung, 2, 118-128 (1969a).

N.M. Aybers & A. Tapucu, Studies on the drag and shape of gas bubbles rising through a stagnant liquid, Wärme- und Stoffübertragung, 2, 171-77 (1969b).

This is the preprint version of a manuscript published in Experimental Thermal and Fluid Science 64 (2015), p. 1-12.
Permalink: http://dx.doi.org/10.1016/j.expthermflusci.2015.01.013

J.R.Grace, T. Wairegi & T.H.Nguyen, Shapes and velocities of single drops and bubbles moving freely through immiscible liquids, Chemical Engineering Research and Design, 54a, 167-173 (1976).

R. Clift , J.R. Grace & M.E. Weber, Bubbles, drops and particles, Academic Press, New York, N.Y. (1978).

G. Ryskin & L.G. Leal, Numerical solution of free-boundary problems in fluid mechanics. Part 2. Buoyancy-driven motion of a gas bubble through a quiescent liquid, J. Fluid Mech., 148, 19-35 (1984).

D.S. Dandy & L.G. Leal, Boundary layer separation from a smooth slip surface, Phys. Fluids, 29, 1360-1366 (1986).

A. Blanco & J. Magnaudet, The structure of the high Reynolds number flow around an ellipsoidal bubble of fixed shape, Phys. Fluids, 7,1265-1274 (1995).

P.C. Duineveld, The rise velocity and shape of bubbles in pure water at high Reynolds number, J. Fluid Mech., 292, 325-332 (1995).

K. Lunde & R. Perkins, Observations on wakes behind spheroidal bubbles and particles, Proc. ASME Fluids Eng. Div. Summer Meeting, Vancouver, Canada, Paper No. FEDSM'97-3530 (1997).

C. Brücker, Structure and dynamics of the wake of bubbles and its relevance for bubble interaction, Phys. Fluids, 11, 1781-1796. (1999).

This is the preprint version of a manuscript published in Experimental Thermal and Fluid Science 64 (2015), p. 1-12.
Permalink: http://dx.doi.org/10.1016/j.expthermflusci.2015.01.013

K. Ellingsen & F. Risso, On the rise of an ellipsoidal bubble in water: oscillatory paths and liquid-induced velocity, J. Fluid Mech., 440, 235-268 (2001).

G. Mougin & J. Magnaudet. Path instability of a rising bubble. Physical review letters, 88(1) (2002).

A.W.G. de Vries, A. Biesheuvel & L. van Wijngaarden, Notes on the path and wake of a gas bubble rising in pure water, International Journal of Multiphase Flow, 28, 1823-1835 (2002).

B. Haut & T. Cartage, Mathematical modeling of gasliquid mass transfer rate in bubble columns operated in the heterogeneous regime, Chemical Engineering Science, 60 (22), 5937-5944 (2005).

W. L. Shew, S. Poncet & J.F. Pinton, Force measurements on rising bubbles, J. Fluid Mech., 569, 51-60 (2006).

G. Mougin & J. Magnaudet, Wake-induced forces and torques on a zigzagging/spiralling bubble, J. Fluid Mech., 567(00), 185-194 (2006).

J. Magnaudet, D. Legendre & G. Mougin, Guillaume, Struggling with Boundary Layers and Wakes of High-Reynolds-Number Bubbles, IUTAM Symposium on Computational Approaches to Multiphase Flow, 81, 263-271 (2006).

J. Magnaudet & G. Mougin, Wake instability of a fixed spheroidal bubble, J. Fluid Mech., 572, 311-337 (2007).

This is the preprint version of a manuscript published in Experimental Thermal and Fluid Science 64 (2015), p. 1-12.
Permalink: http://dx.doi.org/10.1016/j.expthermflusci.2015.01.013

R. Zenit, R. & J. Magnaudet, Path instability of rising spheroidal air bubbles: A shape-controlled process, Phys. Fluids, 20(6) (2008).

C. Wylock, A. Larcy, P. Colinet, T. Cartage & B. Haut, Direct numerical simulation of bubble-liquid mass transfer coupled with chemical reactions: Influence of bubble shape and interface contamination, Colloids and Surfaces A: Physicochemical and Engineering Aspects, 381(1), 130-138 (2011).

D. Legendre, R. Zenit & J.R. Velez-Cordero, On the deformation of gas bubbles in liquids, Phys. Fluids, 24, (2012).

J.C. Cano-Lozano, P. Bohorquez & C. Martínez-Bazán, Wake instability of a fixed axisymmetric bubble of realistic shape, International Journal of Multiphase Flow, 51, 11-21 (2012).

D. Mikaelian, A. Larcy, S. Dehaeck & B. Haut, A new experimental method to analyze the dynamics and the morphology of bubbles in liquids: Application to single ellipsoidal bubbles, Chemical Engineering Science, 100, 529-538 (2013).

R.H. Perry & D.W. Green, Perry's Chemical Engineers' Handbook (7th Edition), McGraw-Hill (1997).

C.S. Ho, Precision of digital vision systems, Pattern Analysis and Machine Intelligence, IEEE Transactions on, 6, 593-601 (1983).

L . W. Bosart & A.O. Snoddy, Ind. Eng. Chem., 20, 1377-1379 (1928).

This is the preprint version of a manuscript published in Experimental Thermal and Fluid Science 64 (2015), p. 1-12.
Permalink: http://dx.doi.org/10.1016/j.expthermflusci.2015.01.013